

THE KINEMATIC STATUS AND MASS CONTENT OF THE SCULPTOR DWARF SPHEROIDAL GALAXY¹

G. BATTAGLIA^{2,3}, A. HELMI³, E. TOLSTOY³, M. IRWIN⁴, V. HILL⁵, P. JABLONKA⁶

Draft version November 1, 2018

ABSTRACT

We present VLT/FLAMES spectroscopic observations ($R \sim 6500$) in the Ca II triplet region for 470 probable kinematic members of the Sculptor (Scl) dwarf spheroidal galaxy. The accurate velocities (± 2 km s⁻¹) and large area coverage of Scl allow us to measure a velocity gradient of $7.6^{+3.0}_{-2.2}$ km s⁻¹ deg⁻¹ along the projected major axis of Scl, likely a signature of intrinsic rotation. We also use our kinematic data to measure the mass distribution within this system. By considering independently the kinematics of the two distinct stellar components known to be present in Scl, we are able to relieve known degeneracies, and find that the observed velocity dispersion profiles are best fitted by a cored dark matter halo with core radius $r_c = 0.5$ kpc and mass enclosed within the last measured point $M(< 1.8 \text{ kpc}) = 3.4 \pm 0.7 \times 10^8 M_\odot$, assuming an increasingly radially anisotropic velocity ellipsoid. This results in a mass-to-light ratio of $158 \pm 33 (M/L)_\odot$ inside 1.8 kpc. An NFW profile with concentration $c = 20$ and mass $M(< 1.8 \text{ kpc}) = 2.2^{+1.0}_{-0.7} \times 10^8 M_\odot$ is also statistically consistent with the observations, but it tends to yield poorer fits for the metal rich stars.

Subject headings: Local Group — galaxies: dwarf — galaxies: Sculptor Dwarf Spheroidal — galaxies: kinematics and dynamics — dark matter

1. INTRODUCTION

Recent wide area photometric and spectroscopic surveys of large numbers of stars in Local Group dwarf spheroidal galaxies (dSphs) have resulted in major progress in our knowledge of these objects and a more complete picture of their characteristics. They appear to be the most dark matter (DM) dominated objects known to date, with mass-to-light (M/L) ratios larger than 100 (e.g., Kleya et al. 2005; Walker et al. 2007, and references therein); their kinematic status is generally believed to be undisturbed by interactions with the Milky Way (MW), with the exception of Carina (see Muñoz et al. 2006, and references therein), Boötes (e.g., Belokurov et al. 2006), and perhaps Ursa Minor (e.g., Bellazzini et al. 2002). In some cases a number of spatial and kinematic substructures have been observed (e.g., Wilkinson et al. 2004; Coleman et al. 2005; Battaglia 2007, hereafter B07), which are perhaps the remnants of accreted subunits (stellar clusters or smaller galaxies). Furthermore, the combination of metallicity ([Fe/H]) and kinematic information have unveiled the presence of multiple stellar components in the Sculptor (Scl) and Fornax dSphs (Tolstoy et al. 2004, hereafter T04; Battaglia et al. 2006), where the metal rich (MR) stars have a more centrally concentrated, less extended spatial distribution, and show colder kinematics than the metal poor (MP) stars.

The presence of multiple stellar populations may require a modification in the way these systems are dynamically mod-

eled to derive their mass content. Traditionally, their mass distribution has been derived from the Jeans analysis of the line-of-sight (l.o.s.) velocity dispersion obtained considering all stars as a single component embedded in an extended DM halo. This analysis is subject to the well known degeneracy between the mass distribution and the orbital motions of the individual stars in the system (mass-anisotropy degeneracy), which prevents a distinction amongst different DM profiles.

In this Letter we show that it is possible to partially break this degeneracy by modeling Scl as a two-(stellar)component system embedded in a DM halo. As part of the modeling of Scl, we also analyzed its dynamical status, and for the first time, we determine the presence of (statistically significant) intrinsic rotation in the stellar component of a dSph.

2. OBSERVATIONS

We acquired photometric data from the ESO/2.2m Wide Field Imager (WFI) at La Silla, and spectroscopic follow-up data in the Ca II triplet (CaT) region from FLAMES at the VLT. Our spectroscopic targets were chosen from the WFI imaging to have the colors and magnitudes consistent with Red Giant Branch (RGB) stars. We acquired data for 15 different fields in Scl (7 fields in addition to those presented in T04). For details of the data reduction and analysis see Battaglia et al. (2006, 2008). From the imaging we obtained the surface density profile of the different stellar populations in Scl and from the spectroscopy we measured line-of-sight (l.o.s.) velocities, and CaT metallicities ([Fe/H]) calibrated using the relation derived in Battaglia et al. (2008).

Using an iterative procedure we measure a systemic velocity $v_{\text{hel,sys}} = 110.6 \pm 0.5$ km s⁻¹ and a dispersion $\sigma = 10.1 \pm 0.3$ km s⁻¹ for Scl. A simple kinematic membership selection (stars with heliocentric l.o.s. velocity within 3σ from $v_{\text{hel,sys}}$) produces 470 probable Scl members, as shown in Fig. 1a. We use this sample when investigating the kinematic status of Scl (Sect. 3), and adopt a more accurate membership criterion when deriving the l.o.s. dispersion profile (Sect. 4).

3. KINEMATIC STATUS AND ROTATION

¹ Based on FLAMES observations collected at the ESO, proposals 171.B-0588 and 076.B-0391A

² Current address: European Organization for Astronomical Research in the Southern Hemisphere; K. Schwarzschild-Str. 2, 85748 Garching, Germany; gbattagl@eso.org

³ Kapteyn Astronomical Institute, University of Groningen, P.O.Box 800, 9700 AV Groningen, the Netherlands; ahelmi, etolstoy@astro.rug.nl

⁴ Institute of Astronomy, Madingley Road, Cambridge CB03 0HA, UK; mike@ast.cam.ac.uk

⁵ GEPI, Observatoire de Paris, CNRS, Université Paris Diderot ; Place Jules Janssen 92190 Meudon, France; Vanessa.Hill@obspm.fr

⁶ Observatoire de Genève, Laboratoire d'Astrophysique de l'École Polytechnique Fédérale de Lausanne (EPFL), CH-1290 Sauverny, Switzerland; Pascale.Jablonka@obs.unige.ch

We first focus on the kinematic status of Scl in terms of tidal disruption and intrinsic rotation, as both these factors can inflate the observed l.o.s. velocity dispersion profile.

No signs of tidal disruption such as tidal tails and S-shaped contours are found in our photometric data-set (Battaglia et al., in prep), although they are not necessarily expected as shown in N-body simulations by Muñoz, Majewski & Johnston (2008). The presence of a velocity gradient along the direction of the galaxy’s orbital motion (indicated by the proper motion direction) is another possible sign of tidal disruption (e.g. Oh, Lin & Aarseth 1995). We will call such a velocity gradient “apparent rotation” to distinguish it from intrinsic rotation. Fig. 1b shows the Galactic standard of rest (GSR) velocities of the probable members of Scl found within ± 0.15 deg from its projected major axis (position angle PA= 99°). At a projected radius $R \sim -0.7$ deg the median velocity is $8.7^{+3.1}_{-4.0}$ km s^{-1} larger than the systemic and at $R \sim +0.5$ deg it is $4.7^{+3.2}_{-3.4}$ km s^{-1} lower. The best-fitting straight-line gives a velocity gradient of $7.6^{+3.0}_{-2.2}$ $\text{km s}^{-1} \text{ deg}^{-1}$. For comparison, no velocity gradients are found along the minor axis (PA= 9°) and other two explored axes at intermediate PA (45° , 135°). Other techniques such as bisection (Walker et al. 2006) support these results. This signal is unlikely to be significantly affected by the foreground since at a projected distance from Scl’s center of 0.5-0.7 deg the expected fraction of MW contaminants in the 3σ membership range is only $\sim 10\%$.

If the measured velocity gradient is caused by tidal disruption, then it should arise along the direction of Scl’s proper motion, which appears not to be the case according to the measurements by Schweitzer et al. (1995) and Piatek et al. (2006). Although the errors on the proper motions are large, it is encouraging that both works agree on the amplitude along the North-South direction, indicating that it is unlikely that more accurate measurements will lead to an orbit aligned with the major axis of Scl. In Fig. 1a we also show the resulting orbits obtained by integrating these proper motions and the l.o.s. velocity of Scl in a Galactic potential. If the tidal debris is aligned with the orbit, then approaching velocities would be detected on the East side of the galaxy, and receding on the West side, opposite to what is observed. Furthermore, the simulations by Muñoz, Majewski & Johnston (2008) also show that velocity gradients due to tidal disruption usually appear at larger projected radii, equal to the King limiting radius (~ 1.3 deg for Scl, see Irwin & Hatzidimitriou 1995) with amplitudes of $\lesssim 2$ km s^{-1} , much smaller than measured here. From these arguments we conclude that it is more likely that the detected velocity gradient is due to intrinsic rotation than to tidal disruption (see Westfall et al. 2006, for a different interpretation based mostly on photometric data). This would therefore be the first time that statistically significant rotation has been found in the stellar component of a dSph.

In the following analysis we use rotation-subtracted GSR velocities. The rotational velocity subtracted to each star is $v_{\text{rot}} = kx$, where $k = -7.6^{+3.0}_{-2.2}$ $\text{km s}^{-1} \text{ deg}^{-1}$ and x is the projected abscissa on the sky.

4. THE MASS CONTENT OF THE SCULPTOR DSPH: TWO STELLAR COMPONENTS MODELING

Scl hosts two stellar populations with distinct spatial, metallicity and kinematic distributions (T04 and references therein). Our spectroscopic sample of RGB stars shows that MR ($[\text{Fe}/\text{H}] > -1.5$) stars are less extended spatially and have

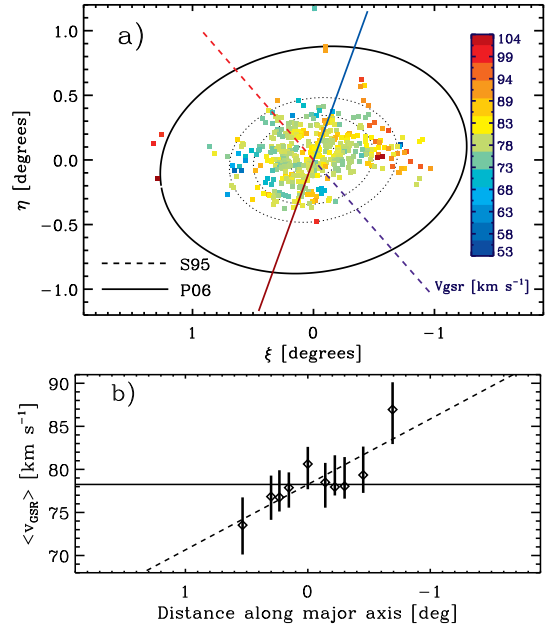


FIG. 1. — a) Velocity field, smoothed with a median filter, for 3σ Scl kinematic members. We use the velocities in the GSR frame to avoid spurious gradients introduced by the component of the Sun and Local Standard of Rest motion’s along the l.o.s. to Scl. The color bar gives the velocity scale. The dotted ellipses are placed at 0.2, 0.5, 0.7 deg to give an idea of the distance scale. The solid ellipse shows the nominal tidal radius (from Irwin and Hatzidimitriou 1995). The dashed and solid lines indicate, respectively, Scl’s orbit calculated using the proper motion measured by Schweitzer et al. (1995) and Piatek et al. (2006), where red and blue shows the receding and approaching velocities. b) Median v_{GSR} per bin versus distance along the projected major axis (diamonds with error-bars) for 3σ Scl kinematic members located within ± 0.15 deg from this axis. Each bin contains ~ 30 stars. The solid and dashed lines show, respectively, Scl systemic velocity and the best fit to the observed velocity gradient (see text). Positive distances correspond to the east side of the galaxy, negative distances to the west side.

colder kinematics than MP ($[\text{Fe}/\text{H}] < -1.7$) stars⁷. MR and MP RGB stars appear to trace, respectively, the Red Horizontal and Blue Horizontal Branch populations (RHB and BHB, respectively), as shown in Figure 2. The number surface density profile of RGB stars from our photometry is well approximated by a two-component fit, where each component is given by the rescaled best-fitting profile derived from our photometry for the RHB and BHB stars.

4.1. Observed Velocity Dispersion Profiles

In the following we derive the observed velocity dispersion profiles of MR and MP RGB stars and use them jointly to constrain the Scl mass content. However, we first need to take into account the presence of MW interlopers which might contaminate our sample and affect the dynamical modeling. The probability of a MW interloper within the 3σ kinematic sample increases with the projected distance from the Scl center as a consequence of the decreasing ratio of the stellar density of Scl versus the MW. As we cannot directly weed out these interlopers using our photometry or spectra we take them into account in a statistical way using a maximum likelihood method.

The probability $P(v_i)$ of observing a star with a velocity v_i and error σ_i at a projected distance from the center $R_1 < R < R_2$, where R_1 and R_2 are a generic inner and outer radius

⁷ We exclude the region $-1.7 < [\text{Fe}/\text{H}] < -1.5$ to limit kinematic contamination between the two populations.

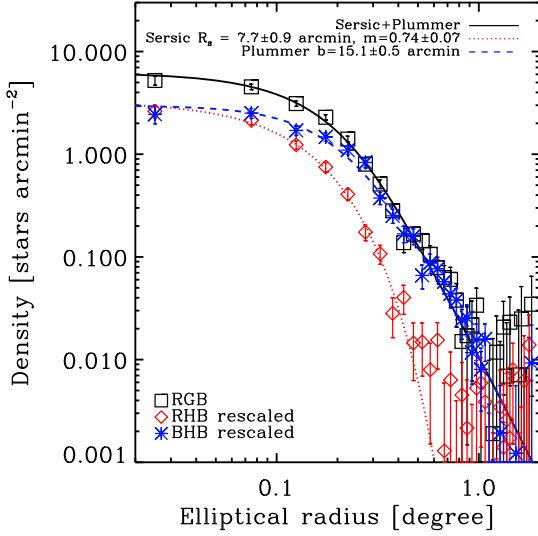


FIG. 2.— Number surface density profile of RGB stars in Scl from ESO/WFI photometry (squares with error-bars) overlaid to the best-fitting two component model (solid line) given by the sum of a Sersic (dotted line) and Plummer (dashed line) profiles. These are obtained from the rescaled profiles that best fit, respectively, the distribution of RHB and BHB stars (diamonds and asterisks with error-bars, respectively) in Scl. The Galactic stellar contamination has been subtracted from each point.

defining an elliptical annulus (distance bin), is:

$$P(v_i | \bar{v}, \sigma) = \frac{N_{\text{MW}}}{N_{\text{T}}} f_{\text{MW}} + \frac{N}{N_{\text{T}}} \frac{e^{-\frac{(v_i - \bar{v})^2}{2(\sigma^2 + \sigma_i^2)}}}{\sqrt{2\pi(\sigma^2 + \sigma_i^2)}}. \quad (1)$$

N_{MW} and N are the expected number of MW and Scl RGB stars in a distance bin ($N_{\text{T}} = N_{\text{MW}} + N$). f_{MW} is the velocity distribution of MW stars, which we assume does not change across the face of Scl, and is derived from the Besançon model (Robin et al. 2003) selecting stars along the l.o.s. and with magnitudes and colors similar to the Scl RGB stars. We assume that the Scl velocity distribution is a Gaussian whose peak velocity \bar{v} and dispersion σ (the quantities we want to derive) are allowed to vary with projected radius. We derive the normalization factors, $N_{\text{MW}}/N_{\text{T}}$ and N/N_{T} directly from the observed RGB surface density profile and relative foreground density. To estimate the fraction of MW interlopers in the MR and MP sub-samples we simply count how many stars with velocities $< v_{\text{sys}} - 3\sigma$ (i.e. the non-membership region more populated by foreground stars) are classified as MR and as MP on the basis of their CaT derived [Fe/H] value. The likelihood of observing a set of velocities v_i with $i = 1, \dots, N$ is $L(v_1, \dots, v_N | \bar{v}, \sigma) = \prod_{i=1}^N P(v_i)$. We maximize the likelihood function in each distance bin and find the corresponding best-fitting $\bar{v}(R)$ and $\sigma(R)$. The errors are determined from the intervals corresponding to 68.3% probability.

The kinematics of the Scl MR and MP RGB stars are clearly different (Figure 3a,b): the l.o.s. velocity dispersion profile of MR stars declines from $\sim 9 \text{ km s}^{-1}$ in the center to $\sim 2 \text{ km s}^{-1}$ at projected radius $R = 0.5 \text{ deg}$, while MP stars are kinematically hotter and exhibit a constant or mildly declining velocity dispersion profile.

4.2. Predicted Velocity Dispersion Profile

The l.o.s. velocity dispersion predicted by the Jeans equation for a spherical system in absence of net-streaming mo-

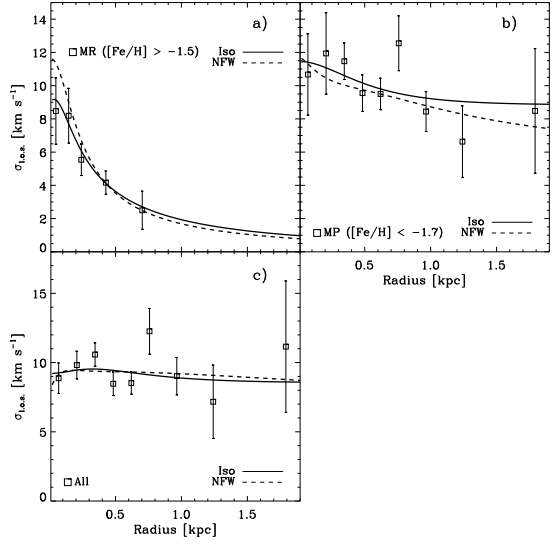


FIG. 3.— l.o.s. velocity dispersion profile (squares with errorbars), from rotation-subtracted GSR velocities, for the MR (a), MP (b) and all (c) RGB stars in Scl. The lines show the best-fitting pseudo-isothermal sphere (solid) and NFW model (dashed) in the hypothesis of $\beta = \beta_{\text{OM}}$. Panel c) shows that the best-fitting pseudo-isothermal sphere with $\beta = \beta_{\text{OM}}$ (solid) and the NFW model with $\beta = \text{const}$ (dashed) are statistically indistinguishable.

tions⁸ is (Binney & Mamon 1982):

$$\sigma_{\text{los}}^2(R) = \frac{2}{\Sigma_*(R)} \int_R^\infty \frac{\rho_*(r) \sigma_{r,*}^2 r}{\sqrt{r^2 - R^2}} (1 - \beta \frac{R^2}{r^2}) dr \quad (2)$$

where R is the projected radius (on the sky), r is the 3D radius. The l.o.s. velocity dispersion depends on: the mass surface density $\Sigma_*(R)$ and mass density $\rho_*(r)$ of the tracer, which in our case are the MR and the MP RGB stars; the tracer velocity anisotropy β , defined as $\beta = 1 - \sigma_\theta^2/\sigma_r^2$, which we allow to be different for MR and MP stars; the radial velocity dispersion $\sigma_{r,*}$ for the specific component, which depends on the total mass distribution (for the general solution see Battaglia et al. 2005).

We consider two DM mass models: a pseudo-isothermal sphere, typically cored, (see Battaglia et al. 2005), and an NFW profile, cusped (Navarro, Frenk & White 1996). Since the contribution of the stars to the total mass of the system is negligible for reasonable stellar M/L ratios, we do not consider it further. As β is unknown we explore two hypotheses: a velocity anisotropy constant with radius, and an Osipkov-Merritt (OM) velocity anisotropy (Osipkov 1979; Merritt 1985). For the latter profile, the velocity anisotropy is $\beta = r^2/(r^2 + r_a^2)$ where r_a is the anisotropy radius.

4.3. Results from the Two-Components Mass Modeling

We explore a range of core radii r_c for the pseudo-isothermal sphere ($r_c = 0.001, 0.05, 0.1, 0.5, 1 \text{ kpc}$) and a range of concentrations c for the NFW profile ($c = 20, 25, 30, 35$). By fixing these, each mass model has two free parameters left: the anisotropy and the DM halo mass (enclosed within the last measured point for the isothermal

⁸ We checked that the assumptions of sphericity and absence of streaming motions have a negligible effect on the results: the observed l.o.s. velocity dispersion profiles derived adopting circular distance bins and not subtracting rotation are consistent at the 1σ level in each bin with the observed l.o.s. velocity dispersion profile derived adopting elliptical binning and by subtracting the observed rotation signal (see B07)

sphere, at $1.3 \text{ deg} = 1.8 \text{ kpc}$ assuming a distance to Scl of 79 kpc, see Mateo 1998; the virial mass for the NFW model). We compute a χ^2 for the MR and MP components separately (χ_{MR}^2 and χ_{MP}^2 , respectively) by comparing the various models to the data. The best-fitting model is obtained by minimizing the sum $\chi^2 = \chi_{\text{MR}}^2 + \chi_{\text{MP}}^2$. We quote as errors in the individual parameters the projections of the $\Delta\chi^2 = 3.53$ region (corresponding to the region of 68.3% *joint* probability for a three free parameters χ^2 distribution).

The models with constant velocity anisotropy yield poor fits for both a cored and a cusped profile. The best-fitting models in the hypothesis of an OM velocity anisotropy are shown in Figure 3a,b and provide very good fits for both the MR and MP components, simultaneously. We find that a pseudo-isothermal sphere with $r_c = 0.5 \text{ kpc}$, $M(< 1.8 \text{ kpc}) = 3.4 \pm 0.7 \times 10^8 M_\odot$, $r_{a,\text{MR}} = 0.2^{+0.1}_{-0.15} \text{ kpc}$ and $r_{a,\text{MP}} = 0.4^{+0.3}_{-0.2} \text{ kpc}$ gives an excellent description of the data ($\chi_{\text{min}}^2 = 6.9$, with $\chi_{\text{MR}}^2 = 0.6$ and $\chi_{\text{MP}}^2 = 6.3$). This gives an M/L ratio for Scl within 1.8 kpc of $158 \pm 33 (M/L)_\odot$, an order of magnitude larger than previous estimates (Queloz, Dubath & Pasquini 1995). Also an NFW model is statistically consistent with the data ($c = 20$, virial mass $M_v = 2.2^{+1.0}_{-0.7} \times 10^9 M_\odot$, $r_{a,\text{MR}} = 0.2 \pm 0.1 \text{ kpc}$ and $r_{a,\text{MP}} = 0.8^{+2.0}_{-0.4} \text{ kpc}$, $\chi_{\text{min}}^2 = 10.8$, with $\chi_{\text{MR}}^2 = 4.2$ and $\chi_{\text{MP}}^2 = 6.6$), but tends to over-predict the central values of the MR velocity dispersion, and this tendency is accentuated for larger concentrations. This model gives a mass within the last measured point of $\sim 2.4^{+1.1}_{-0.7} \times 10^8 M_\odot$, which is consistent with the mass predicted by the best-fitting isothermal sphere model.

Fig. 3c clearly shows the mass-anisotropy degeneracy present when modeling Scl as a single stellar component system: both a cored profile with OM velocity anisotropy and an NFW model with constant velocity anisotropy give a very good fit to the observed l.o.s. velocity dispersion profile, and they are indistinguishable.

5. DISCUSSION AND CONCLUSIONS

We have explored the kinematic status and mass content of the Scl dSph using accurate line-of-sight velocities and CaT

[Fe/H] measurements from VLT/FLAMES spectra of 470 Scl probable members. The large spatial coverage and statistics of this data-set, combined with the accurate velocity measurements, allowed us for the first time to detect in the stellar component of a dSph a statistically significant velocity gradient likely due to intrinsic rotation. This gradient is $7.6^{+3.0}_{-2.2} \text{ km s}^{-1} \text{ deg}^{-1}$ along the Scl projected major axis.

The presence of rotation in dSphs could support scenarios in which the progenitors of these objects were rotationally supported, disky systems, tidally stirred by the interaction with the MW (e.g. Mayer et al. 2001). The efficiency of the transformation from this kind of systems into dSphs, which are spheroidal in shape and have a pressure supported kinematics, is dependent on the eccentricity of the orbit and pericentric distance with respect to the host galaxy. It is likely that objects which have not been efficiently stirred could retain some of their initial kinematic characteristics, such as for example rotation.

Under the hypothesis that Scl is not tidally disrupted we have determined its mass using the Jeans equations, which assume dynamical equilibrium. The combined fit of MR and MP stars allows us to partly relieve the mass-anisotropy degeneracy present in modeling Scl as a single stellar population and to exclude the models with constant velocity anisotropy (Battaglia et al., in preparation). The best-fit is given by a cored profile of $r_c = 0.5 \text{ kpc}$ and mass $M(< 1.8 \text{ kpc}) = 3.4 \pm 0.7 \times 10^8 M_\odot$, assuming that the velocity anisotropy follows an OM model. This result is in a 1.5σ agreement with the results of Strigari et al. (2007), who performed a careful comparison between different systems and datasets, measuring the mass of each galaxy within the same distance from the center. Our result makes Scl more massive than previously thought, and this does not support the conjecture that all dSphs have a common mass scale (Gilmore et al. 2007).

We thank L.Sales for kindly providing the orbits shown in Fig.1.

Facilities: VLT:Kueyen (FLAMES).

REFERENCES

- Battaglia, G., et al. 2005, MNRAS, 364, 433
 Battaglia, G., et al. 2006, A&A, 459, 423
 Battaglia, G. 2007, PhD thesis, Univ. Groningen, The Netherlands, <http://irs.ub.rug.nl/ppn/304002712> (B07)
 Battaglia, G., et al. 2008, MNRAS, 383, 183
 Bellazzini, M., et al. 2002, AJ, 124, 3222
 Belokurov, V., et al. 2006, ApJ, 642, L137
 Binney, J. & Mamon, G. A. 1982, MNRAS, 200, 361
 Coleman, M. G., Da Costa, G. S., Bland-Hawthorn, J., & Freeman, K. C. 2005, AJ, 129, 1443
 Gilmore, G., et al. 2007, ApJ, 663, 948
 Irwin, M. J., & Hatzidimitriou, D. 1995, MNRAS, 277, 1354
 Kleyna, J. T., Wilkinson, M. I., Evans, N. W., & Gilmore, G. F. 2005, ApJ, 630, 141
 Mateo, M. L. 1998, ARA&A, 36, 435
 Mayer, L., et al. 2001, ApJ, 559, 754
 Merritt, D. 1985, MNRAS, 214, 25
 Muñoz, R. R. et al. 2006, ApJ, 649, 201
 Muñoz, R. R., Majewski, S. R., & Johnston, K. V. 2008, preprint (astro-ph/0712.4312)
 Navarro, J. F., Frenk, C. S., & White, S. D. M. 1996, ApJ, 462, 563
 Oh, K. S., Lin, D. N. C., & Aarseth, S. J. 1995, ApJ, 442, 142
 Osipkov, L. P. 1979, Soviet Astronomy Letters, 5, 42
 Piatek, S., et al. 2006, AJ, 131, 1445
 Queloz, D., Dubath, P., & Paquini, L. 1995, A&A, 300, 31
 Robin, A. C., Reylé, C., Derrière, S., & Picaud, S. 2003, A&A, 409, 523
 Schweitzer, A. E., Cudworth, K. M., Majewski, S. R., Suntzeff, N. B. 1995, AJ, 110, 2747
 Strigari, L. E., et al. 2007, ApJ, 669, 676
 Tolstoy, E., et al. 2004, ApJ, 617, 119 (T04)
 Walker, M. G., et al. 2006, AJ, 131, 2114
 Walker, M. G., et al. 2007, ApJ, 667, 53
 Westfall, K. B., et al. 2006, AJ, 131, 375
 Wilkinson, M., et al. 2004, ApJ, 611, 21